

Rheology of Crystallizing LLDPE

Marat Andreev^a, David Nicholson^a, Anthony Kotula^b, Jonathan Moore^c,

Jaap den Doelder^{d,e}, Gregory C. Rutledge^{a*}

^aDepartment of Chemical Engineering, Massachusetts Institute of Technology, Cambridge, MA

^bNational Institute of Standards and Technology, Gaithersburg, MD

^cThe Dow Chemical Company, Midland, MI

^dDow Benelux BV, Terneuzen, The Netherlands

^eLaboratory of Physical Chemistry, Department of Chemical Engineering and Chemistry, Eindhoven University of Technology. Eindhoven, The Netherlands

Abstract

Polymer crystallization occurs in many plastic manufacturing processes, from injection molding to film blowing. Linear low-density polyethylene (LLDPE) is one of the most commonly processed polymers, wherein the type and extent of short-chain branching (SCB) may be varied to influence crystallization. In this work, we report simultaneous measurements of the rheology and Raman spectra, using a Rheo-Raman microscope, for two industrial-grade LLDPEs undergoing crystallization. These polymers are characterized by broad polydispersity, SCB and the presence of polymer chain entanglements. The rheological behavior of these entangled LLDPE melts is modeled as a function of crystallinity using a slip-link model. The partially crystallized melt is represented by a blend of linear chains with either free or crosslinked ends, wherein the crosslinks represent attachment to growing crystallites, and a modulus shift factor that increases with degree of crystallinity. In contrast to our previous application of the slip-link model to isotactic polypropylene (iPP), in which the introduction of only bridging segments with crosslinks at both ends was sufficient to describe the available data, for these LLDPEs we find it necessary to introduce dangling segments, with crosslinks at only one end. The model captures quantitatively the evolution of viscosity and elasticity with crystallization over the whole range of frequencies in the linear regime for two LLDPE grades.

Official contribution of the National Institute of Standards and Technology; not subject to copyright in the United States

1. Introduction

Many manufacturing processes for plastic goods involve the forming and shaping of the polymer melt, and its subsequent crystallization to form the semicrystalline product. Polymer melts are characterized by molecular details such as the molar mass distribution and the degree and type of chain branching. Additionally, long polymer chains are known to form entanglements that strongly affect the polymer dynamics [1]. All of the above factors influence the polymer melt rheology and crystallization kinetics. Moreover, the interplay between flow and crystallization is known to be significant and is frequently exploited in industrial processing. A good example is blown film processing, where the polymer melt is formed by air bubble pressure and flow direction drawing into a thin film. In this process, the polymer melt is cooled by surrounding air after exiting the die. At some point it starts to crystallize while still being formed. Under sufficiently strong flows, crystallization is accelerated since individual polymer chains become stretched and oriented, which leads to a lower entropic barrier for crystallization. This phenomenon is known as flow-induced crystallization (FIC) [2–5]. Similarly, as the material crystallizes and solidifies, its rheological properties change, thereby altering the molecular processes of stretching and orientation. The ability to account for the effects of these molecular details during industrial processing is highly desirable. Particularly, in blown film processing, the solidification of the material determines the overall geometry for the air bubble and the thickness of the final product [6–8].

The rheology of partially crystallized polymers has been studied before. We refer the reader to a previous paper [9] for a recent overview of available experimental observations and modeling approaches. In brief, the rheology of a crystallizing material is usually studied by measuring the dynamic modulus $G^*(\omega)$ over a range of frequencies during crystallization [10–16]. Elastic G' and viscous G'' moduli increase over the full range of frequencies as a material crystallizes, but at different rates for different frequencies, resulting in a change in the shape of the whole $G^*(\omega)$. Notably, G' grows faster than G'' , consistent with the transformation from a visco-elastic fluid to an elastic, solid-like material. From another point of view, if $G^*(\omega)$ is represented as a spectrum of relaxation modes, the individual relaxation times of all modes increase, but the rate of increase is different for each mode [17]. To describe this transformation, two main theoretical approaches have been used. In the first approach, suspension-based two-phase models ascribe the increase of moduli to the growing fraction of solid crystallites, whose moduli are much higher than those of the melt [17–19]. In the second approach, network models interpret the change in relaxation times as a physical crosslinking of polymer chains by the developing crystallites [17].

Experimental measurement of the evolution of the dynamic modulus $G^*(\omega)$ as a function of frequency during crystallization is limited by the time required for a frequency sweep [10–16]. This time is on the order of tens of seconds, which can be large compared to the crystallization timescale. This puts a limitation on the materials and temperatures that can be studied. Some typical ways to work around this issue include: (i) limiting the measurement to relatively high deformation frequencies, where less time is required [16,20]; (ii) limiting experiments to conditions (e.g., temperature) where the crystallization time is much longer than the measurement time [10]; and (iii) using the “inverse quench” wherein the system is first quenched to a low temperature and held for a period of time to allow crystallization, then raised to a temperature at which crystallization proceeds very slowly, while rheological measurements are taken [11,12]. Additionally, comprehensive crystallization studies require simultaneous measurements of both rheology and crystallinity, which typically require specialized equipment [21,22].

One such specialized apparatus is the Rheo-Raman microscope developed by Kotula and coworkers, which offers the ability to measure $G^*(\omega)$ over a wide range of frequencies simultaneously with crystallinity [23]. The Rheo-Raman microscope combines a stress-controlled rheometer with a Raman spectrometer and polarized optical microscope, using a microscope objective that images the sample through a transparent lower plate. The rheometer measures standard viscoelastic properties using small amplitude oscillatory shear (SAOS) while Raman spectra are collected simultaneously. The features of the Raman spectrum are used to calculate the crystallinity of the sample. This method has been used successfully to correlate the complex shear modulus and crystallinity of polycaprolactones [19,24]. The results were modeled using a generalized effective medium theory based on viscoelastic suspensions, which provided a phenomenological description of the crystallization process. Additionally, combined measurements using optical microscopy and SAOS rheometry on crystallizing iPP were well-described by the effective medium model [25]. Although the effective medium model is successful in describing the crystallization process over two orders of magnitude in frequency for those materials, it does not offer a molecular-level description of the crystallization process, with prospects for a first-principles description of the viscoelastic response of a partially crystallized polymer.

In a previous paper [9], we introduced a model that combines features of both suspension and network models and is capable of quantitative description of the rheology of partially-crystallized polymers. The model attributes the growth of dynamic modulus $G^*(\omega)$ over the whole range of frequencies to the fraction of crystallites in the two-phase system, while it changes the shape of $G^*(\omega)$ by adding crosslinks to segments in the melt phase. These crosslinks represent polymer segments attached to crystallites. They permanently constrain the polymer chains and prohibit some relaxation processes, thereby increasing relaxation times. In a first demonstration, the model was successfully applied to data available in the

literature for iPP. Those results showed that during the early stages of crystallization, the rheology could be well-described by a fraction of bridging chains between crystallites. The fraction of bridging chains increased smoothly and monotonically with the crystallinity, while the increase in modulus of the whole two-phase system was captured by the suspension model of Kotula and Migler. [19]. One of the keys to success of the model is its foundation upon the discrete slip-link model (DSM) [26–29], an accurate and flexible computational model for entangled polymer melts that is capable of describing the rheology of entangled and crosslinked polymers simultaneously [30,31].

While there are many good candidates for polymer crystallization studies, herein, we focus on linear low-density polyethylene (LLDPE). It is one of the most common polymers for plastic manufacturing, and it has distinctive properties from low-density polyethylene (LDPE) and high-density polyethylene (HDPE). In particular, it allows for better control over crystallization kinetics. We exploit this feature by comparing two industrial-grade samples with different types of short-chain branches. The Rheo-Raman microscope is used to correlate the rheology and crystallinity for these LLDPEs, and these correlations are captured by the slip-link model for partially crystallized polymer melts. The modeling suggests a difference between the two samples in the structure of their crystallite networks. This difference is reflected in the model through the inclusion of dangling chain segments.

2. Experiment

A. Material Characterization

Two LLDPE samples were studied; both are industrial-grade materials from Dow. Their properties are summarized in Table 1. LLDPE A is a copolymer of ethylene and hexene, resulting in short butyl branches along the chain, and LLDPE B is a copolymer of ethylene and octene, with hexyl branches. While the mass average molar mass M_w of the samples are actually within 20 % of each other, LLDPE B has a broader molar mass distribution, as indicated by the dispersity (D) defined as the ratio of M_w to the number average molar mass M_n .

Table 1. Molecular structure of LLDPE samples studied in this work

	M_w	M_n	D	comonomer	comonomer content (# per 1000 C)
LLDPE A	98.5 kDa	46.2 kDa	2.13	hexene	16
LLDPE B	120 kDa	28.9 kDa	4.14	octene	13

Details of molar mass distribution and comonomer content are shown in Figure 1. Molar mass distributions (Fig. 1a) were obtained by gel permeation chromatography (GPC) (GPC-IR, Polymer Char) [32]. The molar

mass distribution for LLDPE B is noticeably broader than that of LLDPE A. Comonomer content was measured with a technique based on crystallization elution fractionation[33], with improvements aimed at reducing co-crystallization (increasing resolution) and reducing analysis time[34]. This technique assumes a linear relationship between comonomer content and elution temperature. Additionally, the mass average molar mass is measured for each temperature fraction, as shown in Fig 1c. Notably, LLDPE B features a high molar mass fraction with low comonomer content (elution temperature $\approx 100^\circ\text{C}$), sometimes referred to as the “HDPE-like fraction”. This fraction with low comonomer content is completely absent in LLDPE A, as shown in Fig. 1b. Fig. 1c also shows a higher comonomer content in LLDPE B for molar masses below 100 kDa.

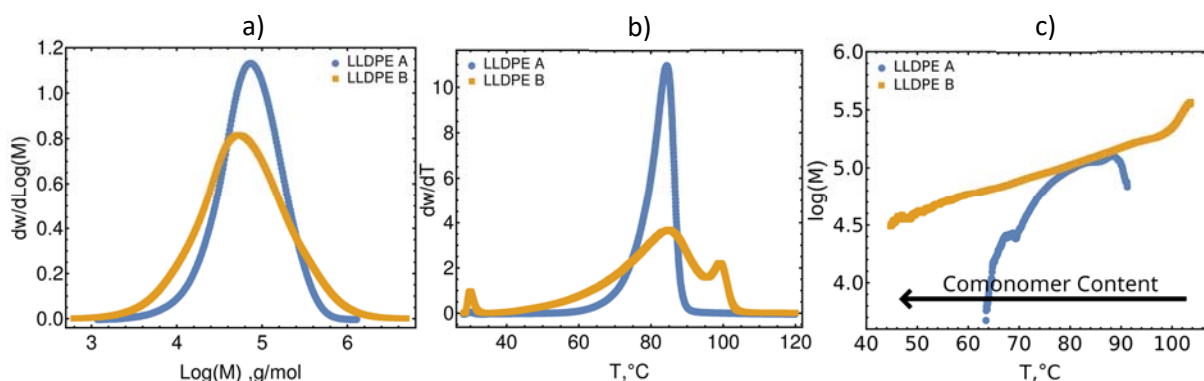


Figure 1. Material characterization of LLDPE A and LLDPE B. a) Molar mass distribution as measured by gel permeation chromatography. b) Comonomer distribution as measured by crystallization elution fractionation. c) Molar mass versus elution temperature (low temperature corresponds to high comonomer content).

B. Rheo-Raman Measurements

Rheo-Raman measurements were performed using an 8 mm diameter parallel plate geometry in a nitrogen environment. The rheo-Raman instrument couples a stress-controlled rheometer (MARS III, Thermo Fisher) with a Raman spectrometer (DXR, Thermo Fisher). Laser excitation from the spectrometer is directed to the base of the rheometer, where a 5x microscope objective (LMPFLN, Olympus) focuses the light into the sample. The backscattered light is collected through the same objective and directed back to the spectrometer for analysis. Details of the instrument are provided in Ref. 23. The plates were heated to 165°C and sample pellets were pressed between the plates to a gap height of 0.6 mm. The pellets were molten for 5 minutes to erase thermal history, and the sample was inspected using the optical microscope on the instrument to confirm that the sample contained no trapped air. The samples were then cooled using a two-stage procedure to minimize undercooling: first, cooling at a rate of $10^\circ\text{C}/\text{min}$ to 10°C above the crystallization temperature T_c , followed by cooling at a rate of $2^\circ\text{C}/\text{min}$ to T_c . The sample was held at T_c while measuring frequency sweeps in the range of 1 rad/s to 100 rad/s with a strain amplitude of 0.004 at a

radius of 4 mm. This strain amplitude is within the linear viscoelastic limit for the samples in both the melt and semicrystalline states, as confirmed by strain sweeps at 1 rad/s (Figure S6 of the Supplementary Information). The frequency range was chosen such that 2 orders of magnitude in relaxation dynamics could be measured multiple times during the crystallization process. Frequency sweeps were chosen instead of multiwave methods to avoid a large total amplitude from the superposition of harmonic modes; the rheometer cannot accept an arbitrary waveform for an optimally-windowed chirp protocol[35]. The T_c values for each resin were identified via trial and error after first performing temperature sweeps in the range of 60 °C to 165 °C (first decreasing temperature, then increasing temperature at a rate of 2 °C/min) with an oscillation frequency of 1 rad/s to find the temperature range where crystallization would occur. Raman spectroscopy measurements were performed using a 5x objective imaging through an optical slit in the rheometer base. The 532 nm laser power was 10 mW, and ten spectra, each with an exposure time of 2 s, were averaged together for each spectrum. The Raman spectra were fit using a series of Voigt peaks in the CH₂ twist and CH₂ bend regions of the spectrum (1200 cm⁻¹ to 1500 cm⁻¹). Examples are shown in the Supplementary Information (Fig. S1). The integrated intensity of the CH₂ bend peak near 1418 cm⁻¹ (I_c) normalized by the total integrated intensity of the CH₂ twist peaks at 1295 cm⁻¹ and 1303 cm⁻¹ (I_{tw}) is proportional to the mass fraction crystallinity χ as measured by differential scanning calorimetry [36,37]. The ratio of the normalized integrated intensity (I_c/I_{tw}) to χ is 0.371 ± 0.012 . The resulting uncertainty in the crystalline mass fraction is 0.015 to 0.025 for the data shown.

Figure 2 shows experimental measurements of crystallinity and rheology during the crystallization of the LLDPEs. In SAOS rheometry, G' and G'' are obtained as the real and imaginary part of the dynamic modulus G^* at a given frequency. During the measurement, SAOS frequencies were cycled through continuously starting from the lowest frequency, resulting in data for crystallinity $\chi(t_c)$, elastic modulus $G'(\omega, t_c)$, and viscous modulus $G''(\omega, t_c)$ for each frequency ω and crystallization time t_c .

Overall, crystallized LLDPE A has a stronger contribution of the elastic component of the dynamic modulus than LLDPE B does. If the crystallized LLDPEs are interpreted simply as crosslinked melts, then LLDPE A would have the higher crosslinking density. However, since the LLDPEs have different molar mass distributions and other molecular characteristics, a quantitative rheological model is required to quantify the crosslinking degree. Moreover, the available information about dynamic modulus for the two materials show distinctive behaviors, which suggests a divergence in crystallite architecture. Therefore, we use a quantitative rheological model that is capable of representing the effect of crystallite architecture on the rheology to establish a connection between the molecular characteristics of melts and the nature of the crystalline network.

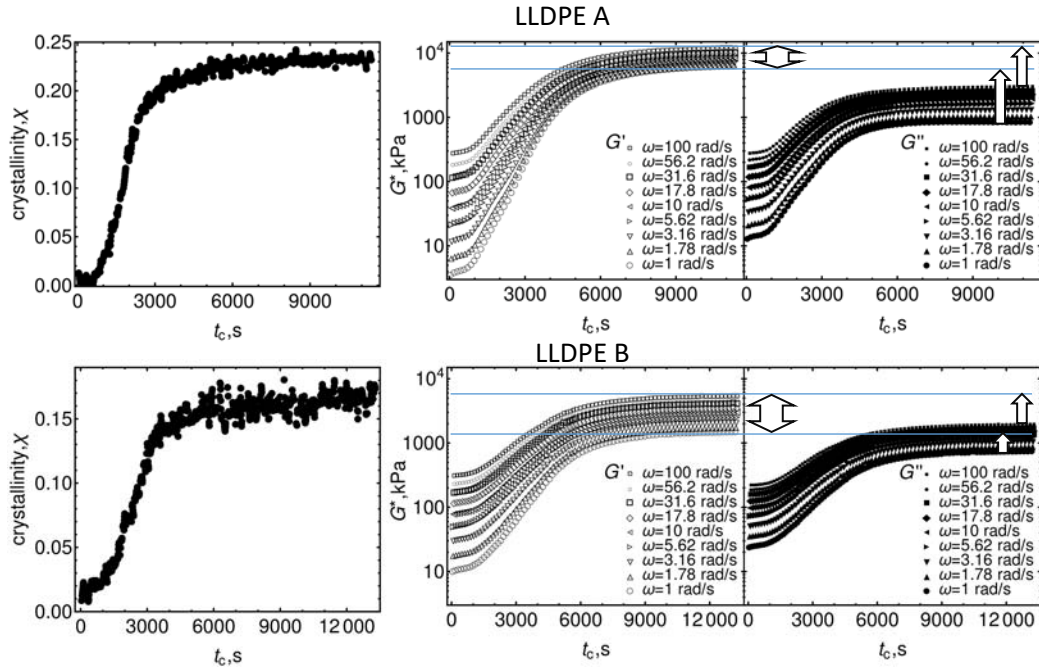


Figure 2. The evolution of crystallinity, elastic modulus G' and viscous modulus G'' during isothermal crystallization of LLDPE melts. Measurements were taken with the Rheo-Raman microscope. Different symbols are different frequencies of SAOS. Crystallization temperature T_c for LLDPE A measurement is 107 °C; for LLDPE B, $T_c = 118^\circ\text{C}$. Blue lines and arrows show the difference between G' and G'' at the lowest and highest frequencies. They highlight a stronger contribution to G' for LLDPE A.

3. Model

A. Slip-link model for partially crystallized polymer melts.

The DSM is a single-chain model – it follows the temporal evolution of a probe chain in the melt and uses slip-links to represent entanglements with other chains. Slip-links limit the movement of the chain and are relaxed by the movement of chain ends [27,28,38]. Since the DSM is a single-chain model, there are two distinct relaxation processes for slip-links. Sliding dynamics (SD) are associated with sliding of the probe chain itself through the slip-links, while constraint dynamics (CD) capture the relaxation (i.e., creation and destruction of slip-links) through the movement of the chains in the background. Since the DSM is a single-chain stochastic model, one simulates an ensemble of probe chains and equates the ensemble averages with macroscopic properties. DSM allows for easy calculation of the dynamics of highly polydisperse polymer melts with entanglements and crosslinks. It is a good candidate for studies of partially crystallized polymer melts, as was illustrated in our previous paper [9].

The concept of the slip-link model for the partially crystallized polymer is illustrated in Fig. 3. The DSM calculations are used for polymer chains in a melt phase of semicrystalline material. Since the DSM is a single chain model, we model different populations of chains separately. Firstly, there are free chains that do not interact with crystallites. Secondly, there are chains partially embedded into a crystallite. In Fig. 3b and Fig. 3c, a crosslink represents a place where the polymer chain is attached to a crystallite. A bridging segment between two crosslinks has an infinitely long relaxation time, similar to a well-crystallized entangled melt. Also, there are “tails”, or dangling segments, with exactly one crosslink per segment located at an end. Such a dangling segment introduces a finite relaxation time that is much longer than that for a free chain of the same length. Previously, such dangling segments were found to be unnecessary to describe the experimental data for iPP. Lastly, we assume that the molar mass distribution of crosslinked chains is the same as that of free chains. We believe that this is a valid assumption for low degrees of crystallinity, where the fraction of chains with more than two crosslinks is negligible. This assumption is re-examined in the Discussion section. For a given crystallinity or crystallization time, the degree of crosslinking is unknown, and therefore we introduce the volume fraction of bridging segments ϕ_B and the volume fraction of dangling segments ϕ_D as adjustable parameters. ϕ_B and ϕ_D have to be specified a priori; therefore multiple trial simulations are required to find their values. Fortunately, as demonstrated shortly, ϕ_B and ϕ_D are found to be monotonic and smooth functions of the degree of crystallinity, so a reasonable initial estimate can be made based on previously completed runs.

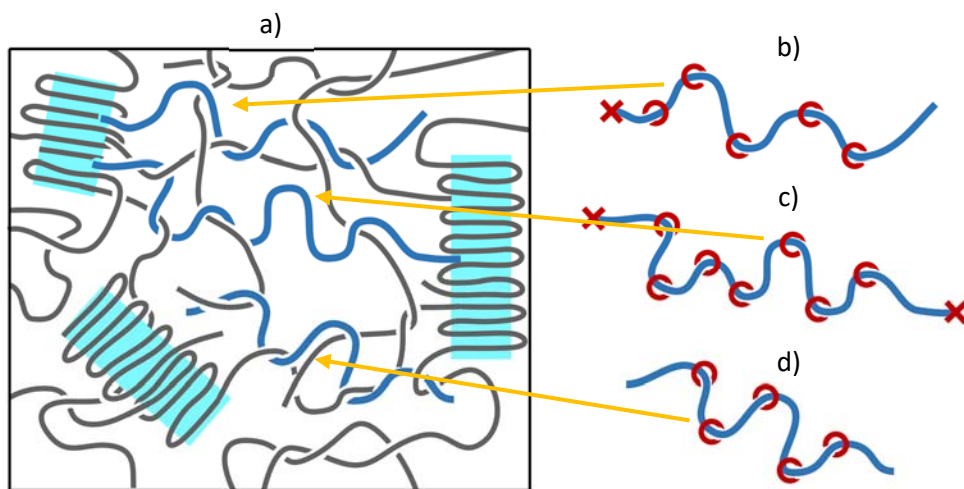


Figure 3. a) A conceptual illustration of the slip-link model for partially crystallized polymer melts. A two-phase material is shown, with the crystallite phase (cyan), the melt phase (white), and probe chains (blue). Several different types of probe chains are considered in the slip-link model: b) dangling chain, crosslinked at one end; c) bridging chain, with crosslinks at both ends; d) free chain, with no crosslinks. Crosslinks (x) represent points of anchoring in a crystalite, and slip-links (O) represent chain-chain entanglements.

While DSM calculations capture the dynamic modulus of the constrained melt component, the rigidification due to the crystallites is taken into account through the modulus shift factor G_{sh} . Solid crystallites have a high modulus and increase the observed modulus over the whole range of frequencies. In this work, G_{sh} is also treated as an adjustable parameter, but it should correlate positively with degree of crystallinity, or time of crystallization. It is simply a scalar multiplicative factor that can be applied a posteriori to simulated moduli across the entire frequency range to shift the results vertically to accord with experiments.

In this study, we apply the DSM for linear chains to a LLDPE melt with SCB. The DSM focuses primarily on entanglement dynamics. Therefore, the critical parameter is the molecular weight of branches compared to the entanglement molecular weight. In this study, the molecular weight of side branches is 57 Da for LLDPE A, and 85 Da for LLDPE B. The entanglement molecular weight is 1100Da for LLDPE A, and 1250Da for LLDPE B. Therefore, side branches are unentangled, and there is no need to represent them explicitly on the level of description of the DSM. On the other hand, the presence of side branches does affect the dynamics and relaxation of the backbone. This effect can be taken into account within the slip-link model by modification of the τ_K value, which is the timescale of sliding a chain segment through a slip-link. Since LLDPE A and LLDPE B have different SCB, we allowed different τ_K values for these two materials. Finally, the SCB modifies the plateau modulus and entanglement molecular weight, as was shown by Fetters et al.[39]

The procedures for finding core DSM parameters (M_e , τ_K) are the same as in our previous work [9]; they are found by fitting to G^* at small crystallization times (≈ 100 s), where crystallinity and crosslinks are negligible. One noteworthy difference from our previous work on iPP is the treatment of polydispersity. For the LLDPEs modeled in this work, full GPC data are available (Fig. 1a). Based on the resolution of that data, two hundred and twelve (212) molar mass modes were used to represent CD in the background chain distribution of LLDPE A, and 264 molar mass modes were used for LLDPE B. A smaller number of modes (13) was used for the probe chains in each case; these were chosen carefully based on their contribution to the total G^* and their computational cost, following Taletsky et al. [40]. The whole ensemble contained 975 probe chains: 325 free chains, 325 dangling chains and 325 bridging chains. Parameterization of one G^* curve took about 130 hours using 325 cores of Intel Xeon E5-2690 processors running at 2.9 GHz. The length of simulation time is determined by the probe chains with the highest molar mass.

The DSM implementation of constraint dynamics relies on an analytical approximation of lifetime distribution[27]. The constraint dynamics for the polydisperse blend is constructed as a superposition of constraint dynamics for individual components, as described in Taletsky et al. [40]. The notable difference

is the presence of dangling and bridging chain components. The analytical form of constraint dynamics for dangling chains is found and presented in Fig. S5. Bridging chains do not contribute to constraint dynamics since crosslinks block their chain ends. Summarizing our approach, first, the DSM is fitted to the rheology of an entangled melt prior to the crystallization, and the DSM parameters (M_e , τ_K) are found. These parameters are then kept fixed and do not change as crystallization proceeds. Secondly, for each time at which data is measured experimentally, a fraction of bridges ϕ_B and a fraction of dangling chains ϕ_D are introduced into the stochastic ensemble of DSM. The shift factor G_{sh} is applied a posteriori to the G^* curves to shift them vertically, to match the experimental data. ϕ_B , ϕ_D and G_{sh} are freely adjustable parameters and are treated as functions of the crystallization time.

B. Slip-link modeling results

The slip-link model is typically compared to experiment through the dynamic modulus $G^*(\omega)$; therefore, it is convenient to convert data acquired in the form of Fig. 2 to a series of $G^*(\omega)$ curves. Since each data point in Fig. 2 corresponds to its own crystallization time, interpolation between nearest data points is necessary to calculate the dynamic modulus $G^*(\omega, t_c)$ at the chosen crystallization times t_c . Using linear interpolation, it is possible to obtain the dynamic modulus $G^*(\omega, t_c)$ for any crystallization time t_c and apply the slip-link model to it. However, in the interest of computational expediency, only 12 crystallization times were selected for each LLDPE. All dynamic modulus curves $G^*(\omega, t_c)$ and corresponding slip-link calculations are shown in the Supplementary Information (Fig. S2 and Fig. S3). Here, we focus on $G^*(\omega)$ curves which highlight significant changes in rheology of LLDPE A and LLDPE B during the crystallization.

The experimental data in Figure 4 shows that LLDPE A transitions from a viscoelastic liquid to an elastic solid over the course of the rheo-Raman experiment. At the beginning of the crystallization run, the G' and G'' of LLDPE A and LLDPE B both exhibit crossover but with weak scaling of G' and G'' vs ω due to broad polydispersity. After approximately 2900 s of crystallization time, LLDPE A exhibits a second crossover at the low end of the frequency range. Generally, the presence of a second crossover in polymer systems is indicative of chain-chain interactions that constrain dynamics in addition to entanglements, such as the case in associating polymers [41]. The position of the second crossover depends on the density of such interactions and their relaxation time. The two crossovers merge at 3.162 rad/s and disappear after a crystallization time of 3200 s. The evolution of crossovers is presented separately in figure S4. After that, the separation between G' and G'' increases inversely to the frequency at low frequencies, suggesting that

no new crossover would likely be observed at still lower frequencies beyond the experimentally accessible range; the material behaves as a solid with no terminal relaxation time.

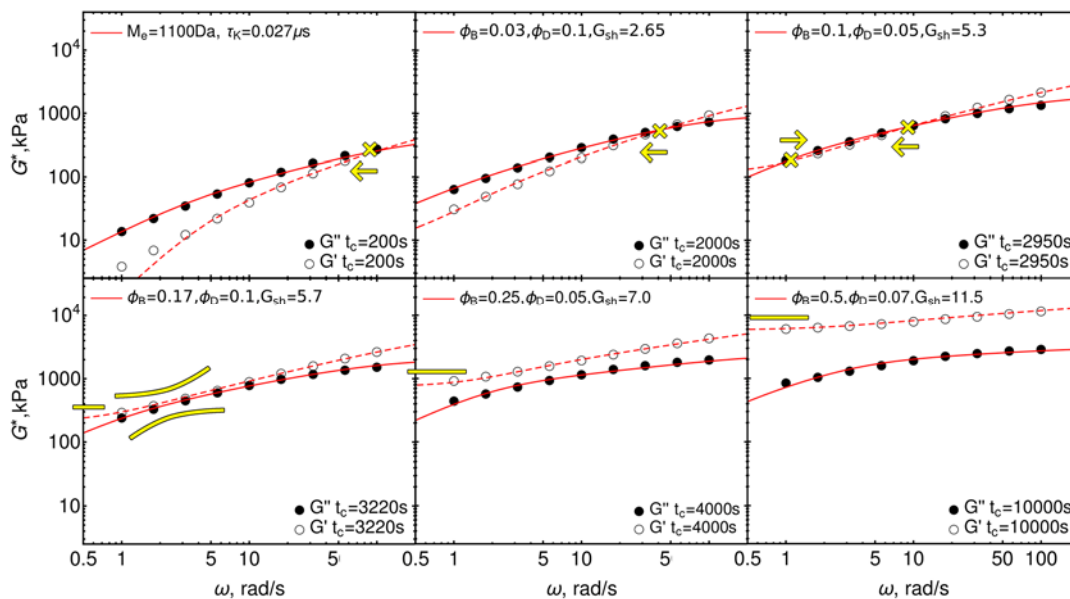


Figure 4. Application of the slip-link model for partially crystallized melt to evolution of dynamic modulus G^* during crystallization of LLDPE A at $T_c=107^\circ\text{C}$. G' (open symbols) and G'' (filled symbols) are experimental data plotted as functions of frequency in SAOS for six different times of isothermal crystallization. Red lines are slip-link calculations. The crossover points between G' and G'' are highlighted (x's), as well their shifts (arrows) during crystallization. Here, crossover points disappear by merging. Also highlighted is the low-frequency slope of G' at the end of crystallization.

Right before crossovers disappear, the G' and G'' both show a power-law dependence on frequency over a range of frequencies. This behavior is described by Winter and coworkers [13,14] as characteristic of polymer materials near the gelation point. As shown below, for the slip-link model, the emergence of the power-law region corresponds to the maximum of the dangling chain fraction, and the fraction of bridging chains transitions from slow to rapid growth right around this point. Therefore, for LLDPE A, the power-law region signifies an important point in the formation of a percolated crystallite network.

The solid curves in Fig. 4 show the fit of the slip-link model to the rheology of LLDPE A during crystallization. LLDPE A was modeled using $M_e = 1100$ Da and $\tau_K = 0.027$ μs . After a crystallization time of 3500 s, the low-frequency plateau observed for LLDPE A is similar to that observed previously for crystallization of iPP [9]. The large fraction of the bridging chains in LLDPE A indicates that a percolated network of crystallites formed at the early stages of crystallization and steadily grew as crystallization continued. Unlike iPP, however, the slip-link calculation for LLDPE A also included a fraction of dangling chains that serve to capture better the rheology at intermediate crystallization times. Overall, the slip-link model captures the rheological data for all crystallization times. As shown by the experimental data in

Figure 5, the rheology of LLDPE B differs significantly from that of LLDPE A during crystallization. When a polymer material undergoes crosslinking with time, G' tends to become relatively insensitive to frequency. Firstly, Fig. 5 shows that G' for LLDPE B is more sensitive to frequency than was the case for LLDPE A. Secondly, there is a smaller separation between G' and G'' for LLDPE B than for LLDPE A. Finally, for LLDPE B the single crossover point simply shifts leftward and exits the experimental frequency range after 4500s. The separation between G' and G'' is almost constant at low frequencies, so it is hard to make a confident assertion about the existence of an additional crossover point at low frequencies outside of the experimentally accessible range.

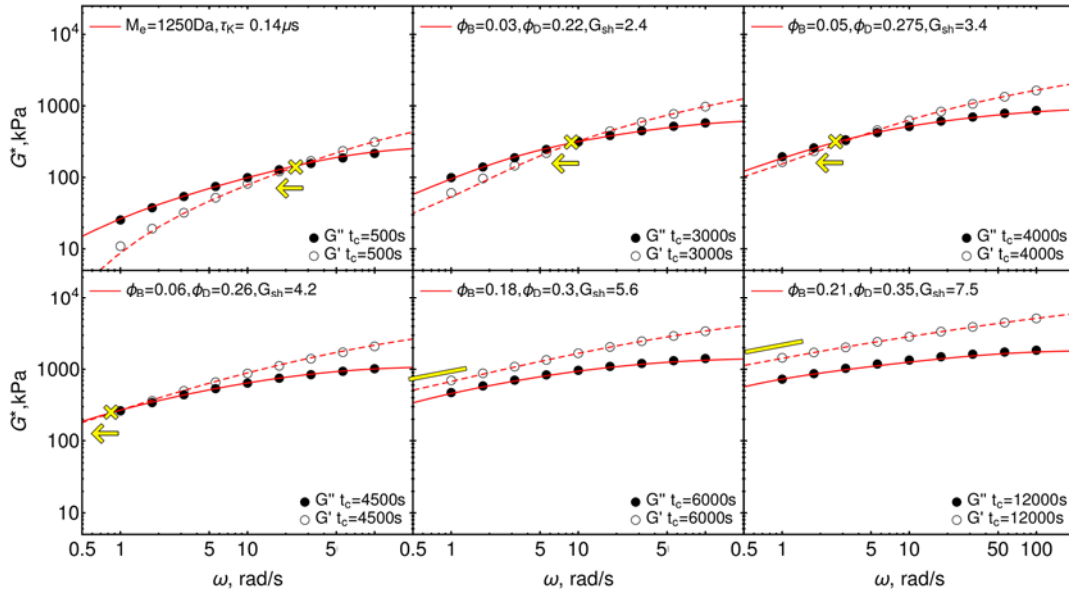


Figure 5. Application of the slip-link model for a partially crystallized melt to the evolution of dynamic modulus G^* during crystallization of LLDPE B at $T_c = 118$ °C. G' (open symbols) and G'' (filled symbols) are experimental data plotted as functions of frequency in SAOS for six different times of isothermal crystallization. Red lines are slip-link calculations. The crossover point between G' and G'' is highlighted (x's), as well its shift (arrows) during crystallization. For LLDPE B, the crossover point exits the experimental window to the left (low frequency) with increasing time (crystallinity). Also highlighted are the low-frequency slopes of G' at the end of crystallization.

The solid curves in Fig. 5 show the fits of the slip-link model to the rheology of LLDPE B during the crystallization. LLDPE B melt rheology has lower plateau modulus than LLDPE A, and therefore the slip-link model captures it using a lower entanglement density. The slip-link model parameters are $M_e = 1250$ Da and $\tau_K = 0.14$ μ s. The ratio of entanglement molecular weights between LLDPE A and LLDPE B is in qualitative agreement with Fetters et al.[39], but slightly larger (1.12 instead of 1.04).. The fraction of dangling chains grows rapidly at low crystallinity and remains significant even at later stages of crystallization. The fraction of bridging chains grows rapidly at intermediate crystallinities, but it is always lower than in LLDPE A. The G' and G'' show dependence on frequency close to power-law behavior for

LLDPE B near the disappearance of crossover. Similar to LLDPE A, its emergence corresponds to the point where the fraction of bridging chains transitions from slow to rapid growth.

In summary, LLDPE melts can exhibit different rheological behaviors during crystallization. Fortunately, DSM for partially crystallized melts is robust enough to capture them. Both bridging and dangling chains are necessary, in addition to applying the G_{sh} factor, to capture the rheology during the crystallization of LLDPEs. The fraction of bridging chains ϕ_B , the fraction of dangling chains ϕ_D and the shift factor G_{sh} evolve smoothly and continuously with crystallization degree. A detailed discussion of these parameters is presented next.

4. Discussion.

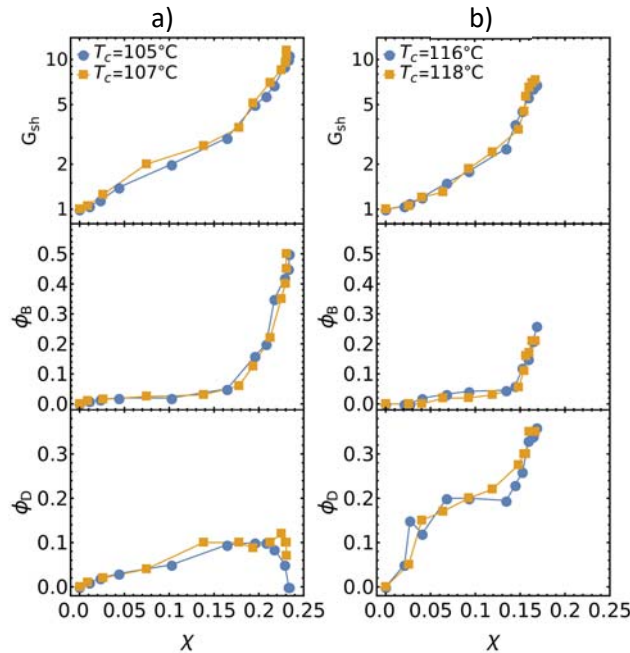


Figure 6. Slip-link parameters for rheology during crystallization of a) LLDPE A, and b) LLDPE B. Fraction of bridging chains ϕ_B , fraction of dangling chains ϕ_D and shift factor G_{sh} are shown. Each set of subfigures shows slip-link parameters for experiments at two crystallization temperatures: $T_c = 105^\circ\text{C}$ and $T_c = 107^\circ\text{C}$ for LLDPE A, and $T_c = 116^\circ\text{C}$ and $T_c = 118^\circ\text{C}$ for LLDPE B.

Experiments show that LLDPE A and LLDPE B exhibit different evolutions in their rheology during crystallization, which the slip-link model captures through different fractions of free, dangling and bridging chains, plus a modulus shift factor. Measurements by rheo-Raman microscopy allow a direct correspondence between the values of the slip-link model parameters and the crystallinity. The variation of the parameters of the slip-link model as a function of crystallinity are shown in Figure 6. ϕ_B is comparable for LLDPE A and LLDPE B for crystallization degrees $\chi < 0.15$, but then ϕ_B increases more quickly with χ in LLDPE B (starting at $\chi \sim 0.15$ instead of ~ 0.2 and with steeper slope), but in LLDPE A it

increases to a greater extent (to a magnitude of 0.5 instead of 0.3). Meanwhile, ϕ_D remains small for LLDPE A and saturates around 0.13, or possibly even decreases, while in LLDPE B ϕ_D continues to increase throughout the duration of the crystallization experiment. G_{sh} curves have similar trends for LLDPE A and LLDPE B. G_{sh} values are very close for crystallization degrees $\chi < 0.15$. At $\chi = 0.15$, G_{sh} for LLDPE B is greater than G_{sh} for LLDPE A. As the crystallinity increases beyond that point, LLDPE B reaches a maximum crystallinity around 0.16 while LLDPE A crystallizes further and ultimately reaches higher G_{sh} values.

The assumption of same molar mass distribution may affect the values obtained for ϕ_B and ϕ_D . A modified molar mass distribution for crosslinked chains would result in different relaxation times, necessitating different values of ϕ_B, ϕ_D to capture the experimental dynamic modulus. However, well-crystallized LLDPE A shows a low-frequency plateau, while LLDPE B does not. Therefore, the dynamic moduli between well-crystallized LLDPE A and LLDPE B are qualitatively different. In our opinion, it is unlikely that radically different ratios of ϕ_B and ϕ_D would be able to capture this feature.

There are several possible explanations for these observations of parameter variation with crystallinity. The first is that the molar mass distribution is different between LLDPE A and LLDPE B. However, available characterization information suggests that differences in the molar mass distributions cannot explain the different trends in ϕ_B and ϕ_D . LLDPE A has the lower M_w and smaller D of the two materials; therefore, based on these considerations, it would have the smaller fraction of long chains that would likely bridge between crystallites. A second possible explanation lies in the different crystallization temperatures for the two experiments. LLDPE A was crystallized at $T_c = 107$ °C while LLDPE B was crystallized at $T_c = 118$ °C. Generally, deeper undercooling, or lower crystallization temperature, leads to more nucleation events and smaller crystallites (i.e., thinner lamellae). However, while crystallization temperatures differ, the crystallization rates are comparable in a sense that full crystallization takes 10000's of seconds for both LLDPEs. This behavior is indeed consistent with a physical interpretation of the parameters of the slip-link model, where LLDPE A crystallizes at a lower temperature than LLDPE B and is characterized by more bridging chains and fewer dangling chains, but has a comparable shift factor. Moreover, Fig. 6 shows slip-link calculations capturing an additional LLDPE B experiment at $T_c = 116$ °C. The slip-link model shows similarly high dangling chain fraction and low bridging chain fraction for LLDPE B. The bridging chain fraction is slightly higher at $T_c = 116$ °C. Assuming linear dependences for ϕ_B and ϕ_D on T_c , it is clear that at $T_c = 107$ °C, LLDPE B would have a different rheology from LLDPE A due to a high dangling chain fraction. Further, Fig. 6 also shows slip-link calculation capturing an additional LLDPE A experiment at $T_c = 105$ °C. Again, the dangling chain fraction and low bridging chain fraction are similar to the experiment at $T_c = 107$ °C, and extrapolating them to $T_c = 118$ °C would not yield

values similar to LLDPE B. Although, an extrapolation over 11 °C based on 2 °C is questionable, we believe the discrepancy is large enough, based on the available data, to conclude that a temperature dependence of bridging and dangling segment populations is not mainly responsible for the deviation in rheology during the crystallization of LLDPE A and LLDPE B.

A third explanation lies in the higher comonomer content and HDPE-like fraction in LLDPE B. Compared to LLDPE A, the SCB in LLDPE B is very asymmetrically distributed, resulting in a high molar mass fraction with very few branches, and a low molar mass fraction with a disproportionately large number of branches. One would expect that the unbranched HDPE-like component crystallizes first, since these segments have fewer “defects” (i.e., short-chain branches that are excluded from the crystal) and can form thicker lamellae that are stable at higher temperatures. This HDPE-like component could be responsible for the high temperature at which crystallization is measured in the Rheo-Raman microscope in LLDPE B. However, since the HDPE-like fraction is small, the nucleation density at this temperature should also be small. We further speculate that ethylene sequences of the SCB-containing molecules are subsequently incorporated into the HDPE-like crystallites, but only partially, resulting in more dangling segments and lower ultimate degree of crystallinity. By comparison, crystallization in LLDPE A is measured at a lower temperature, where thinner lamellae are stable, and even shorter ethylene sequence lengths can crystallize. Furthermore, since nucleation in LLDPE A is not dependent on a small fraction of unbranched segments, more nuclei are formed, and they are more homogeneously distributed in the material. Therefore, LLDPE A forms a larger fraction of bridging chains. Additionally, smaller SCB content results in a lower fraction of dangling chains in the melt phase of LLDPE A.

The second and third explanations are not mutually exclusive. LLDPE B crystallizes at higher temperature because of its HDPE-like content, and the resulting partially crystallized melt comprises only a low number density of crystallites at this temperature. These crystallites subsequently grow by addition of chains with SCB, but otherwise remain few and far apart, characterized by small bridging fraction and large dangling fraction. In contrast to LLDPE B, in LLDPE A branches are distributed more uniformly, so deeper undercooling is required to initiate crystallization and, the crystallites are correspondingly smaller and more numerous. Thus, one observes more bridging between these crystallites, and fewer dangling segments, in LLDPE A. Thus, the key difference in this case is the different number and size of crystallites that arise due to crystallization at very different undercoolings, which in turn can be attributed to the availability of segments with low branching content to initiate crystallization at higher temperature.

Finally, the modulus shift factor G_{sh} is different between LLDPE A and LLDPE B, suggesting some difference in crystallite structure. While ϕ_B and ϕ_D capture modifications of the melt component of semicrystalline material, G_{sh} depends first and foremost on degree of crystallinity. However, differences

in G_{sh} between LLDPE A and LLDPE B appear for $\chi > 0.15$, indicative of some secondary influence, possibly related to morphology [19,24,25]. One possible explanation is a dimensional effect related to the size or shape of the crystallites; crystallites with higher aspect ratios might be expected to interact more strongly at modest degrees of crystallinity. Another possible explanation is a dimensional effect related to the distance between crystallites. If the distance between crystallite surfaces becomes smaller than the extent of dangling chains, the interaction between crystallites would become stronger, due to interactions between dangling chains on different crystallites. For the thicker and larger crystallites covered with dangling chains in LLDPE B, this dimensional effect appears at $\chi \cong 0.15$, while for the thinner and smaller crystallites in LLDPE A, this effect is postponed to $\chi \cong 0.2$.

4. Conclusion

In summary, we have measured simultaneously the rheology and degree of crystallinity of two LLDPE melts as they undergo crystallization using a Rheo-Raman microscope. The rheology is captured in the form of dynamic modulus G^* over a range of frequencies spanning two orders of magnitude, allowing us to follow closely the increase in total modulus and changes in relaxation times during solidification. The rheological modulus is complemented by measurements of crystallinity. Therefore, changes in viscoelastic behavior can be connected to the degree of crystallization of the material. The two LLDPEs are broadly polydisperse and are similar in terms of mass average molar mass and melt state rheology, but differ in comonomer type and SCB content and crystallize to a material with different rheological properties.

The slip-link model for partially crystallized entangled polymer melts is used to describe the data for LLDPE A and LLDPE B during crystallization. A modulus shift factor, a fraction of bridging segments with crosslinks at both ends and, for the first time, a fraction of dangling segments with crosslinks at only one end are included in the stochastic ensemble and suffice to capture the gradual increase in relaxation time during crystallization of these LLDPEs. The model is shown to be capable of describing the behavior of these industrial grade LLDPEs quantitatively.

The slip-link model developed in this work interprets the increase in relaxation time of the melt as a result of physical crosslinking between crystallites and the increase in total modulus primarily as the result of the increasing volume fraction of solid crystallites. A close examination of these parameters of the model, in particular the fractions of bridging and dangling chains, offers insight into the different behaviors of LLDPE A and LLDPE B. The results from the slip-link model suggest that different number densities and sizes of crystallites are formed in these two materials. This result is consistent with expectations based on the temperatures at which crystallization is observed in the two LLDPEs and with their different distributions of SCB content. Therefore, this study demonstrates that it is feasible to relate rheology during

crystallization to the molecular architecture of the polymer (e.g., molar mass distribution and SCB). Ultimately, with additional data, we hope it will be possible to solve the inverse problem of predicting the evolution of bridging and dangling chain fractions during crystallization from information on molecular architecture alone.

Supplementary Material

Raman spectra and peak deconvolution of LLDPE B during crystallization at 116 °C; full sets of slip-link model fits to the dynamic modulus G^* during crystallization for LLDPE A and LLDPE B; G' and G'' crossover frequency during the crystallization of LLDPE A and LLDPE B; details of dangling chain constraint dynamics implementation; strain sweeps of LLDPE A and LLDPE B in the melt and semicrystalline states.

Acknowledgments

We gratefully acknowledge partial support from Dow through the University Partnership Initiative. Anthony Kotula would like to thank Kalman Migler and Chad Snyder for helpful discussions. Certain commercial equipment, instruments, or materials are identified in this paper in order to adequately specify experimental procedure. Such identification does not imply recommendation or endorsement by the National Institute of Standards and Technology, nor does it imply that the materials or equipment identified are necessarily the best available for the purpose.

- [1] Doi, M., and S. F. Edwards. "Dynamics Of Concentrated Polymer Systems Part I." *J. Chem. Soc. Faraday Trans. 2 Mol. Chem. Phys.* **74**, 1789–1801 (1978).
- [2] Peters, G. W. M., L. Balzano, and R. J. A. Steenbakkers. "Flow-Induced Crystallization." *Handb. Polym. Cryst.* 399?432 (2013). <https://doi.org/10.1002/9781118541838.ch14>.
- [3] Kumaraswamy, G. "Crystallization of Polymers from Stressed Melts." *J. Macromol. Sci. - Polym. Rev.* **45**, 375–397 (2005). <https://doi.org/10.1080/15321790500304171>.
- [4] Graham, R. S. "Modelling Flow-Induced Crystallisation in Polymers." *Chem. Commun.* **50**, 3531–3545 (2014). <https://doi.org/10.1039/c3cc49668f>.
- [5] Janeschitz-Kriegl, H. *Crystallization Modalities in Polymer Melt Processing*; (2018). <https://doi.org/10.1007/978-3-319-77317-9>.
- [6] Pirkle, J. J. C., and R. D. Braatz. "A Thin-Shell Two-Phase Microstructural Model for Blown Film

- Extrusion.” *J. Rheol.* (N. Y. N. Y). **54**, 471–505 (2010). <https://doi.org/10.1122/1.3366603>.
- [7] Pirkle, J. J. C., and R. D. Braatz. “Dynamic Modeling of Blown-Film Extrusion.” *Polym. Eng. Sci.* **43**, 398–418 (2003). <https://doi.org/10.1002/pen.10033>.
- [8] Housiadas, K. D., G. Klidis, and J. Tsamopoulos. “Two- and Three-Dimensional Instabilities in the Film Blowing Process.” *J. Nonnewton. Fluid Mech.* **141**, 193–220 (2007). <https://doi.org/10.1016/j.jnnfm.2006.09.006>.
- [9] Andreev, M., and G. C. Rutledge. “A Slip-Link Model for Rheology of Entangled Polymer Melts with Crystallization.” *J. Rheol.* (N. Y. N. Y). **64**, 213–222 (2020). <https://doi.org/10.1122/1.5124383>.
- [10] Pantani, R., V. Speranza, and G. Titomanlio. “Simultaneous Morphological and Rheological Measurements on Polypropylene: Effect of Crystallinity on Viscoelastic Parameters.” *J. Rheol.* (N. Y. N. Y). **59**, 377–390 (2015). <https://doi.org/10.1122/1.4906121>.
- [11] Acierno, S., and N. Grizzuti. “Measurements of the Rheological Behavior of a Crystallizing Polymer by an ‘Inverse Quenching’ Technique.” *J. Rheol.* (N. Y. N. Y). **47**, 563–576 (2003). <https://doi.org/10.1122/1.1545080>.
- [12] Coppola, S., S. Acierno, N. Grizzuti, and D. Vlassopoulos. “Viscoelastic Behavior of Semicrystalline Thermoplastic Polymers during the Early Stages of Crystallization.” *Macromolecules* **39**, 1507–1514 (2006). <https://doi.org/10.1021/ma0518510>.
- [13] Pogodina, N. V., and H. H. Winter. “Polypropylene Crystallization as a Physical Gelation Process.” *Macromolecules* **31**, 8164–8172 (1998). <https://doi.org/10.1021/ma980134l>.
- [14] Pogodina, N. V., V. P. Lavrenko, S. Srinivas, and H. H. Winter. “Rheology and Structure of IPP near Gel Point: Quiescent and Shear-Induced Crystallization.” *Polymer (Guildf)*. **42**, 9031–9043 (2001).
- [15] Pogodina, N. V., S. K. Siddiquee, J. W. Van Egmond, and H. H. Winter. “Correlation of Rheology and Light Scattering in Isotactic Polypropylene during Early Stages of Crystallization.” *Macromolecules* **32**, 1167–1174 (1999). <https://doi.org/10.1021/ma980737x>.
- [16] Roozmond, P. C., V. Janssens, P. van Puyvelde, and G. W. M. Peters. “Suspension-like Hardening Behavior of HDPE and Time-Hardening Superposition.” *Rheol. Acta* **51**, 97–109 (2012). <https://doi.org/10.1007/s00397-011-0570-1>.

- [17] Steenbakkers, R. J. A., and G. W. M. Peters. “Suspension-Based Rheological Modeling of Crystallizing Polymer Melts.” *Rheol. Acta* **47**, 643–665 (2008). <https://doi.org/10.1007/s00397-008-0273-4>.
- [18] Christensen, R. M., and K. H. Lo. “Solutions for Effective Shear Properties in Three Phase Sphere and Cylinder Models.” *J. Mech. Phys. Solids* **27**, 315–330 (1979). [https://doi.org/10.1016/0022-5096\(79\)90032-2](https://doi.org/10.1016/0022-5096(79)90032-2).
- [19] Kotula, A. P., and K. B. Migler. “Evaluating Models for Polycaprolactone Crystallization via Simultaneous Rheology and Raman Spectroscopy.” *J. Rheol. (N. Y. N. Y.)* **62**, 343–356 (2018). <https://doi.org/10.1122/1.5008381>.
- [20] Boutahar, K., C. Carrot, and J. Guillet. “Crystallization of Polyolefins from Rheological Measurements - Relation between the Transformed Fraction and the Dynamic Moduli.” *Macromolecules* **31**, 1921–1929 (1998). <https://doi.org/10.1021/ma9710592>.
- [21] Roozmond, P. C., M. van Drongelen, L. Verbelen, P. Van Puyvelde, and G. W. M. Peters. “Flow-Induced Crystallization Studied in the RheoDSC Device: Quantifying the Importance of Edge Effects.” *Rheol. Acta* **54**, 1–8 (2015). <https://doi.org/10.1007/s00397-014-0820-0>.
- [22] Plog, J. P., M. Meyer, F. De Vito, F. Soergel, and A. Kotula. “Rheo-Raman Microscope: Tracking Molecular Structures as a Function of Deformation and Temperature.” *AIP Conf. Proc.* **1736**, (2016). <https://doi.org/10.1063/1.4949647>.
- [23] Kotula, A. P., M. W. Meyer, F. De Vito, J. Plog, A. R. Hight Walker, and K. B. Migler. “The Rheo-Raman Microscope: Simultaneous Chemical, Conformational, Mechanical, and Microstructural Measures of Soft Materials.” *Rev. Sci. Instrum.* **87**, 105105 (2016). <https://doi.org/10.1063/1.4963746>.
- [24] Kotula, A. “A Frequency-Dependent Effective Medium Model for the Rheology of Crystallizing Polymers.” *J. Rheol. (N. Y. N. Y.)* **64**, 505–515 (2020). <https://doi.org/10.1122/1.5132407>.
- [25] Roy, D., D. J. Audus, and K. B. Migler. “Rheology of Crystallizing Polymers: The Role of Spherulitic Superstructures, Gap Height, and Nucleation Densities.” *J. Rheol. (N. Y. N. Y.)* **63**, 851–862 (2019). <https://doi.org/10.1122/1.5109893>.
- [26] Schieber, J. D., J. Neergaard, and S. Gupta. “A Full-Chain, Temporary Network Model with Sliplinks, Chain-Length Fluctuations, Chain Connectivity and Chain Stretching.” *J. Rheol. (N. Y. N. Y.)* **47**, 213–233 (2003). <https://doi.org/10.1122/1.1530155>.

- [27] Khaliullin, R. N., and J. D. Schieber. “Self-Consistent Modeling of Constraint Release in a Single-Chain Mean-Field Slip-Link Model.” *Macromolecules* **42**, 7504–7517 (2009).
<https://doi.org/10.1021/ma900533s>.
- [28] Andreev, M., H. Feng, L. Yang, and J. D. Schieber. “Universality and Speedup in Equilibrium and Nonlinear Rheology Predictions of the Fixed Slip-Link Model.” *J. Rheol. (N. Y. N. Y.)* **58**, 723–736 (2014). <https://doi.org/10.1122/1.4869252>.
- [29] Andreev, M., and J. D. Schieber. “Accessible and Quantitative Entangled Polymer Rheology Predictions, Suitable for Complex Flow Calculations.” *Macromolecules* **48**, 1606–1613 (2015).
<https://doi.org/10.1021/ma502525x>.
- [30] Katarova, M., M. Andreev, Y. Sliozberg, R. A. Mrozek, J. L. Lenhart, J. W. Andzelm, and J. D. Schieber. “Rheological Predictions of Network Systems Swollen with Entangled Solvent.” *AICHE J.* **60**, 1372–1380 (2014). <https://doi.org/10.1002/aic>.
- [31] Jensen, M. K., R. Khaliullin, and J. D. Schieber. “Self-Consistent Modeling of Entangled Network Strands and Linear Dangling Structures in a Single-Strand Mean-Field Slip-Link Model.” *Rheol. Acta* **51**, 21–35 (2012). <https://doi.org/10.1007/s00397-011-0568-8>.
- [32] Moore, J. C. “Gel Permeation Chromatography. I. A New Method for Molecular Weight Distribution of High Polymers.” *J. Polym. Sci. Part A Gen. Pap.* **2**, 835–843 (1964).
<https://doi.org/10.1002/pol.1964.100020220>.
- [33] Monrabal, B., J. Sancho-Tello, N. Mayo, and L. Romero. “Crystallization Elution Fractionation. A New Separation Process for Polyolefin Resins.” *Macromol. Symp.* **257**, 71–79 (2007).
<https://doi.org/10.1002/masy.200751106>.
- [34] Hollis, C., A. Parrott, R. Cong, and M. Cheatham. “Chromatography of Polymers with Reduced Co-Crystallization.” WO2017040127, 2017.
- [35] Geri, M., B. Keshavarz, T. Divoux, C. Clasen, D. J. Curtis, and G. H. McKinley. “Time-Resolved Mechanical Spectroscopy of Soft Materials via Optimally Windowed Chirps.” *Phys. Rev. X* **8**, 41042 (2018). <https://doi.org/10.1103/PhysRevX.8.041042>.
- [36] Migler, K. B., A. P. Kotula, and A. R. Hight Walker. “Trans-Rich Structures in Early Stage Crystallization of Polyethylene.” *Macromolecules* **48**, 4555–4561 (2015).
<https://doi.org/10.1021/ma5025895>.
- [37] Strobl, G. R., and W. Hagedorn. “Raman Spectroscopic Method for Determining the Crystallinity

- of Polyethylene.” AIP Conf Proc **16**, 1181–1193 (1978).
<https://doi.org/10.1002/pol.1978.180160704>.
- [38] Schieber, J. D., and M. Andreev. “Entangled Polymer Dynamics in Equilibrium and Flow Modeled Through Slip Links.” *Annu. Rev. Chem. Biomol. Eng.* **5**, 367–381 (2014).
<https://doi.org/10.1146/annurev-chembioeng-060713-040252>.
- [39] Fetters, L. J., D. J. Lohse, C. A. García-Franco, P. Brant, and D. Richter. “Prediction of Melt State Poly(α -Olefin) Rheological Properties: The Unsuspected Role of the Average Molecular Weight per Backbone Bond.” *Macromolecules* **35**, 10096–10101 (2002).
<https://doi.org/10.1021/ma025659z>.
- [40] Taletskiy, K., T. A. Tervoort, and J. D. Schieber. “Predictions of the Linear Rheology of Polydisperse, Entangled Linear Polymer Melts by Using the Discrete Slip-Link Model.” *J. Rheol. (N. Y. N. Y.)*. **62**, 1331–1338 (2018). <https://doi.org/10.1122/1.5033858>.
- [41] Shivokhin, M. E., T. Narita, L. Talini, A. Habicht, S. Seiffert, T. Indei, and J. D. Schieber. “Interplay of Entanglement and Association Effects on the Dynamics of Semidilute Solutions of Multisticker Polymer Chains.” *J. Rheol. (N. Y. N. Y.)*. **61**, 1231–1241 (2017).
<https://doi.org/10.1122/1.4997740>.